Unattached kinetochores rather than intrakinetochore tension arrest mitosis in taxol-treated cells

Valentin Magidson,[1]* Jie He,[1]* Jeffrey G. Ault,[1] Christopher B. O'Connell,[1] Nachen Yang,[1] Irina Tikhonenko,[1] Bruce F. McEwen,[1,2] Haixin Sui,[1,2] and Alexey Khodjakov[1,3]

[1]Wadsworth Center, New York State Department of Health, Albany, NY 12201
[2]School of Public Health, State University of New York, Albany, NY 12201
[3]Rensselaer Polytechnic Institute, Troy, NY 12180

Kinetochores attach chromosomes to the spindle microtubules and signal the spindle assembly checkpoint to delay mitotic exit until all chromosomes are attached. Light microscopy approaches aimed to indirectly determine distances between various proteins within the kinetochore (termed Delta) suggest that kinetochores become stretched by spindle forces and compact elastically when the force is suppressed. Low Delta is believed to arrest mitotic progression in taxol-treated cells. However, the structural basis of Delta remains unknown. By integrating same-kinetochore light microscopy and electron microscopy, we demonstrate that the value of Delta is affected by the variability in the shape and size of outer kinetochore domains. The outer kinetochore compacts when spindle forces are maximal during metaphase. When the forces are weakened by taxol treatment, the outer kinetochore expands radially and some kinetochores completely lose microtubule attachment, a condition known to arrest mitotic progression. These observations offer an alternative interpretation of intrakinetochore tension and question whether Delta plays a direct role in the control of mitotic progression.

Introduction

The dynamic interactions between microtubules of the mitotic spindle and chromosomes are mediated by kinetochores. These organelles are essential for chromosome segregation and control of mitotic progression (Cheeseman, 2014; Sacristan and Kops, 2015). Both molecular composition and structural organization of kinetochores change as the spindle assembles and matures. The kinetochore size decreases noticeably as several checkpoint proteins and molecular motors are released on formation of end-on microtubule attachments (Thrower et al., 1996; Hoffman et al., 2001; Magidson et al., 2015; Wynne and Funabiki, 2015). As these attachments mature, kinetochore composition continues to change (Manning et al., 2010), but direct visualization of corresponding structural changes is challenging because of the small size of attached kinetochores. In conventional light microscopy (LM), kinetochores appear as small spots that lack discernable features. In EM, attached kinetochores are described as 200-nm-wide and ∼75-nm-thin discs comprising three distinct domains: an electron translucent layer sandwiched between the outer and inner electron-opaque layers, each ∼25-nm thick (Brinkley and Stubblefield, 1966; Rieder, 1982).

Inability to directly visualize nanometer-scale changes in the kinetochore architecture by LM has inspired the use of indirect approaches. Single-molecule high-resolution colocalization (SHREC) in which molecular distances between proteins are inferred from the separation of fluorescent spots (Churchman and Spudich, 2012) has been used to map the locations of all major complexes within the kinetochore and reveal the changes that allow kinetochores to satisfy the mitotic checkpoint (Wan et al., 2009; Maresca and Salmon, 2010; Suzuki et al., 2011; Varma et al., 2013). Although formally applicable only to single molecules, SHREC could be valid for kinetochores if the thin layered disc morphology of the organelle remains constant under various physiologic conditions and experimental treatments. However, the assumption that kinetochore morphology is constant under varied conditions has not been validated.

By using correlative LM/EM analyses and superresolution LM, we demonstrate a high degree of variability in kinetochore architecture in human cells. The outer kinetochore domain is compact during metaphase when the spindle forces are maximal, but it expands radially when microtubule dynamics are suppressed by taxol. Nanometer-scale distributions of various kinetochore components are complex and do not resemble the layered-disc morphology expected in the interpretation of SHREC. Further, the values of Delta are strongly affected

The Rockefeller University Press $30.00
J. Cell Biol. Vol. 212 No. 3   307–319
www.jcb.org/cgi/doi/10.1083/jcb.201412139

JCB   **307**

by the degree of structural preservation achieved during fixation. These results suggest that Delta is not a reliable metric for distances between various molecules within mammalian kinetochores. Instead, in addition to distances between various molecules, Delta reflects supramolecular changes in the kinetochore architecture. Furthermore, we find that cells with low-stretch kinetochores induced by the treatment with taxol exit from mitosis unless some of the kinetochores become completely detached from microtubules. Unattached kinetochores recruit the checkpoint protein Mad2, which is known to be sufficient for arresting mitotic progression. Therefore, the current concept of intrakinetochore tension and its role in the control of mitotic progression may need to be reconsidered.

Results

Taxol treatment results in changes in the orientation of the kinetochore outer layer

To directly correlate SHREC and structural organization at the EM resolution, we stain the outer kinetochore protein Hec1 with FluoroNanogold-conjugated antibodies, which delineates the kinetochore outer layer in both LM (fluorescence) and EM (gold particles). Analyses are conducted in RPE1 cells with GFP-tagged centrioles (Centrin1-GFP) and inner kinetochores (CenpA-GFP; Magidson et al., 2011). The combination of a centrosome and two kinetochore markers in a single cell allows us to determine the distance between the centroids of Hec1 and CenpA fluorescence within individual kinetochores (i.e., SHREC Delta; Wan et al., 2009), the orientations of individual centromeres within the spindle (cTilt), and the orientations of individual kinetochores with respect to their centromeres (kTilt; Fig. 1, A and B; and Fig S1, A–C). Further, by superimposing Hec1 fluorescence on the distribution of gold particles in the corresponding EM images, we determine the orientation of individual kinetochores with respect to the attached microtubule bundles (K fibers; Fig. S1, B and C). Ten untreated metaphase cells (361 chromosomes) and five metaphase cells (117 chromosomes) treated with the microtubule-stabilizing drug taxol for ∼15 min are analyzed.

Chromatic aberration because of the variable flatness and optical thickness of preparations presents a major obstacle in SHREC analyses. Two alternative approaches to compensating chromatic aberration have been proposed for SHREC on kinetochores (Wan et al., 2009). In the first approach, measurements are obtained for pairs of sister kinetochores, and Delta is calculated on the assumption that chromatic shifts are negated for sister kinetochores oriented in opposite directions (Fig. 1 B, method I). This approach assigns the same Delta to both kinetochores. However, live-cell recordings reveal uncorrelated fluctuations of Delta in sister kinetochores (Uchida et al., 2009; Dumont et al., 2012). A high level of dissimilarity in the distribution of gold particles within sister kinetochores (Fig. S1 C) also suggests that sister kinetochores are not structurally equal. Therefore, pairwise calculations of Delta are not suited for correlative LM/EM investigations aimed to reveal the structural basis of changes in Delta.

Chromatic aberration can be compensated on the expectation that the mean values of Delta are similar in the populations of kinetochores oriented toward opposite spindle poles (i.e., the spindle is overall symmetric; Wan et al., 2009). Indeed, in raw images, the populations of left versus right kinetochores in the same cell appear statistically different (Fig. S1, D and E), but they become similar if one channel is shifted so that the global centers of mass for the red and green channels coincide (Fig. S1, D′ and E′). Therefore, a subpixel-scale translation of the channels appears to compensate for chromatic aberration, which in turn enables direct measurements of Delta for individual kinetochores (Fig. 1 B, method II). Both methods are expected to yield identical results (Wan et al., 2009), and indeed the mean values of Delta$_{CenpA-GFP–Hec1}$ are similar in metaphase RPE1 cells (140 vs. 143 nm, P = 0.016). However, in taxol-treated cells, the difference between Delta values obtained by the alternative methods is highly significant (91 vs. 109 nm, P < 0.0001; Fig. 1 C).

A potential explanation for the observed discrepancy between the results produced by method I versus method II is that both the mean value and variability of kTilt appear to increase significantly (P < 0.0001) in taxol-treated cells (Fig. 1 D). This indicates that internal axes of sister kinetochores are no longer antiparallel, i.e., kinetochores become disoriented with respect to the centromere axis. Such a disorientation would result in an illusory decrease in Delta when calculations involve projection of K–K$_{CenpA}$ distance on the K–K$_{Hec1}$ axis (method I). To determine whether the observed differences in Delta values are numerically consistent with the increase in kTilt, we constructed a computer simulation that compares the output of method I versus method II for cells with various spindle/centromere geometries and various values of chromatic aberration. Importantly, the model considers not only the mean values but also their variability. The latter is inherent in a complex organelle such as a kinetochore. As illustrated in Fig. S2, method I is sensitive to the variability in kTilt. In contrast, method II is not affected by angular flexibility within the centromere; however, this method is inaccurate when the mean value of Delta is smaller than two SDs of the distribution. Under this condition, values produced by method II are affected by both the mean and variability in intrakinetochore distances. For two spatially coincident but independent markers, direct measurements should converge on ∼78% of the SD. Indeed, direct measurements of kinetochores in metaphase cells stained for Hec1 in both green and red channels yield Delta values of –3 ± 7 nm by Method I and 16 ± 9 nm by method II (Fig. S2 A; *n* = 106 chromosomes in three cells). These values are not statistically different from the predictions of the model. The differences in Delta values obtained by the alternative approaches in control versus taxol-treated metaphases are also consistent with the model (Fig. S2 A). Therefore, our experimental results can be explained by the taxol-induced loss of proper orientation of the kinetochores with respect to the centromere.

Kinetochores have been portrayed as distinct trilaminar plates, but serial section EM reveals a large degree of morphologic variability among kinetochores identified via correlations with CenpA-GFP fluorescence in LM. This approach prevents biased selection of kinetochores with the expected morphology and demonstrates that even perfectly coplanar sister kinetochores often lack discernable plates (Fig. S3 A). To gain insight into the typical shape of the outer layer, we averaged LM and EM images of the same kinetochores aligned by the orientation of the attached K fibers (see Materials and methods). Cumulative distributions of gold particles in the populations of aligned kinetochores suggest that during metaphase the outer layer of a typical kinetochore does resemble a plate orthogonal to the attached K fiber (Fig. 2). In contrast, the distribution of Hec1 in taxol-treated cells is larger and more rounded (the depth of the
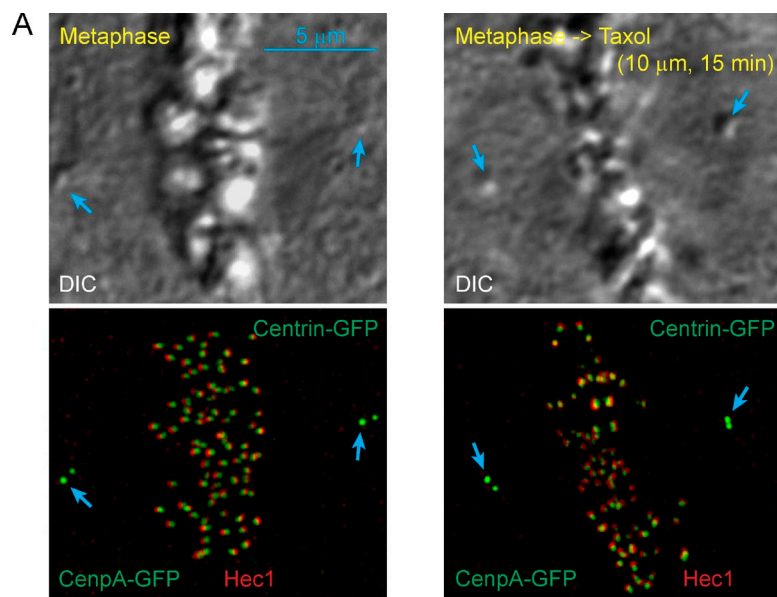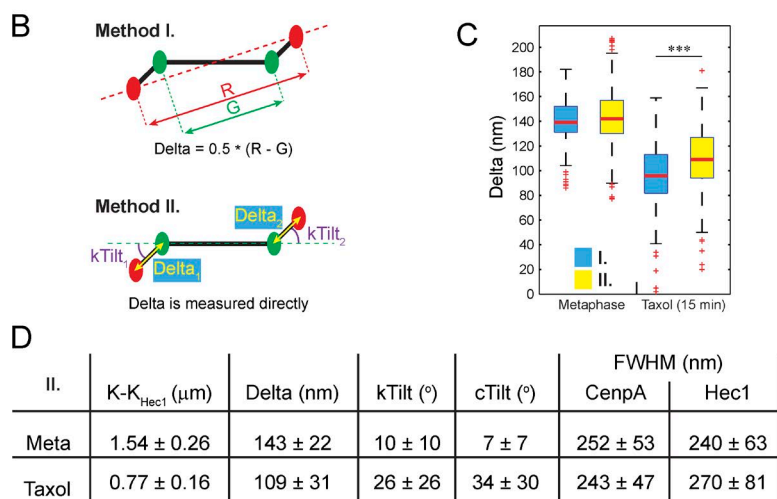
Figure 1. **Alternative approaches to compensation of chromatic aberration lead to different Delta values in taxol-treated cells.** (A) DIC images (top) and maximum intensity projections (bottom) of control and taxol-treated RPE1 cells in metaphase. Inner and outer layers of kinetochores are labeled using CenpA-GFP expression (green) and immunostaining for Hec1 (Fluoro-NanoGold, red). Spindle poles (centrioles) are labeled using expression of Centrin1-GFP (blue arrows). (B) Diagrams illustrating two alternative methods for calculating Delta measurements developed by Wan et al. (2009). Method I: pairwise calculations of sister kinetochores based on projecting inner kinetochore spots onto the axis determined by the outer kinetochore spots; method II: direct measurement of Delta after global chromatic correction based on the assumption that the spindle is symmetric overall. (C) Box plots presenting the values of Delta calculated by method I versus method II. ***, P < 0.001 in two-tailed *t* test. (D) Mean values ± SD for various parameters of kinetochore organization calculated by method II.

II.	K-K$_{Hec1}$ (μm)	Delta (nm)	kTilt (°)	cTilt (°)	FWHM (nm) CenpA	FWHM (nm) Hec1
Meta	1.54 ± 0.26	143 ± 22	10 ± 10	7 ± 7	252 ± 53	240 ± 63
Taxol	0.77 ± 0.16	109 ± 31	26 ± 26	34 ± 30	243 ± 47	270 ± 81

distribution is similar to its width). This enlargement observed in the EM space is consistent with the statistically significant increase in the full width at half-maximum (FWHM) observed after taxol treatment in LM for Hec1 (P < 0.00001) but not CenpA-GFP (P = 0.109) fluorescence (Fig. 1 D).

Analysis of the aligned kinetochores reveals that orientation of the kinetochores with respect to the attached K fiber differs in metaphase versus taxol-treated cells. In metaphase, CenpA centroids of aligned kinetochores cluster directly behind Hec1 on the axis of K-fiber microtubules as expected if the plates are orthogonal to the attached K fibers (Fig. 2 B″). In contrast, the position of CenpA centroids is variable in taxol-treated cells (Fig. 2 B″). Because the orientation of the attached K fibers and the positions of Hec1 centroids are fixed in the aligned datasets, variability in the positions of CenpA centroids represents variability in the orientation of the CenpA-Hec1 axis with respect to the centromere axis (i.e., kTilt). Therefore, the EM data are consistent with the changes in kTilt observed in the SHREC analyses. To summarize, the two major changes in kinetochore architecture induced by taxol are expansion of the outer, but not the inner, layer and variability in the orientation of the intrakinetochore axis with respect to the centromere axis.

Metaphase kinetochores with large Delta display distorted plates

Immunogold analysis demonstrates that the cumulative distribution of Hec1 is ~200 nm deep, even in untreated metaphase cells (Fig. 2 B′). This suggests a large variability in the shape of the kinetochore outer plate, which is consistent with EM observations in cells that have not been permeabilized for immunostaining (Fig. S3 A). Therefore, we sought to investigate whether the value of Delta correlates with the shape of the outer layer.

We conduct correlative LM/EM analysis on RPE1 cells that express CenpA-GFP and Mis12-mCherry (Fig. 3, A and B; three cells). Tagging both the inner and outer kinetochore components with fluorescent proteins allows us to determine Delta and the kinetochore shape without the disruption of structure associated with the permeabilization required for immunostaining. We choose Mis12 to assess the proximal surface of the kinetochore outer layer to avoid the potential perturbation of the kinetochore structure due to the overexpression of the fluorescently labeled Hec1 because this protein directly binds to the attached microtubules. Correlative LM/EM analyses of 28 kinetochores suggest that kinetochores with low Delta are flat or lack a clearly delineated plate, whereas the plates of highly stretched kinetochores appear distorted (Fig. S3 C). To gain
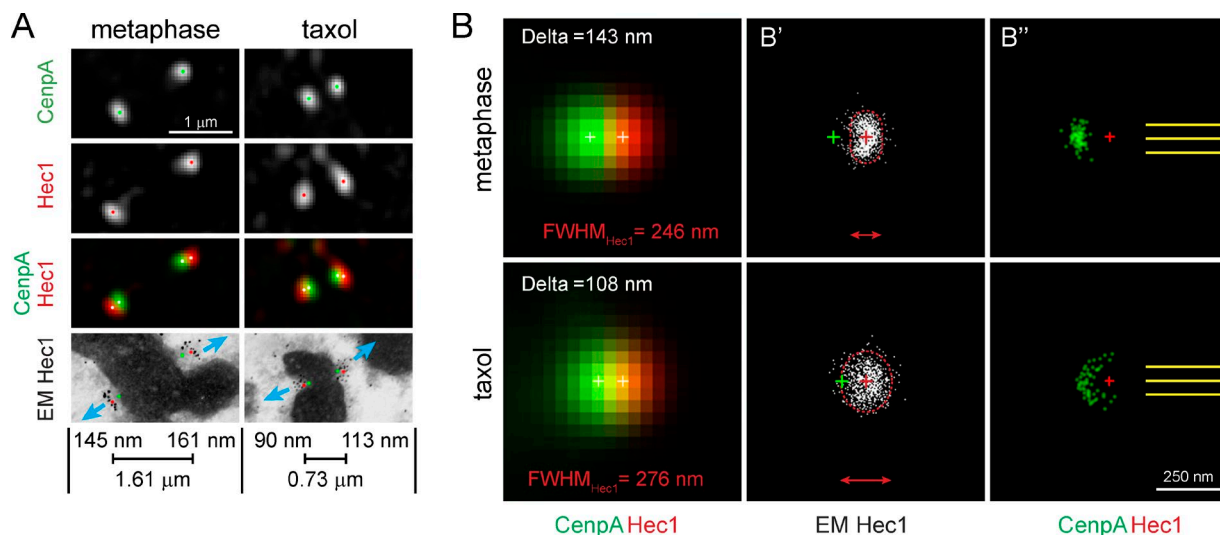
Figure 2. **Expansion of the outer kinetochore in taxol-treated cells.** (A) Representative kinetochores from metaphase and taxol-treated cells. Positions of CenpA-GFP and Hec1 centroids are marked by green and red dots, respectively, and white dots on the dual-color image. Blue arrows denote orientation of K fibers. Notice variability in the shape of gold-particle clusters between sister kinetochores in immuno-EM images. Delta values for each kinetochore and interkinetochore stretch (Hec1–Hec1) are shown. (B and B″) Averaged images of aligned kinetochores in metaphase ($n = 90$, four cells) and taxol-treated ($n = 60$, three cells). (B) Delta and FWHM$_{Hec1}$ values directly measured in the averaged fluorescent images are indicated. Notice a close match between these values and mean values shown in Fig. 1 D. Centroids CenpA-GFP and Hec1 fluorescence are indicated by white crosses. (B′) Cumulative distribution of gold particles in immuno-EM images of control and taxol-treated metaphase kinetochores. Notice the difference in shape and size of the Hec1 distributions. Dashed boundaries enclose 90% of gold particles. Red and green crosses denote centroids of Hec1 and CenpA-GFP fluorescence (B″) Positions of CenpA-GFP centroids (green dots) relative to fixed centroids of Hec1 (red crosses) and the orientation of the microtubule bundles (yellow lines). CenpA centroids are tightly clustered during metaphase but are spread in taxol-treated cells.

additional insight into the shape of high- versus low-stretch kinetochores, we used EM tomography to reconstruct sections that contained central parts of 14 of these kinetochores.

Repeated measurements of the same kinetochore in sequential images of glutaraldehyde-fixed cells demonstrate that reliable classification of individual kinetochores as stretched versus collapsed is possible only when the measured Deltas differ by >20 nm (Fig. S3, C and D). Therefore, kinetochores with Deltas <25 or >55 nm were chosen for tomography.

Tomography analysis confirmed that kinetochores with high Delta display distorted outer plates with protuberances directed away from the chromatin (Fig. 3, B and C). By calculating positions of the center of mass for the full volume of the plate and after masking the protuberances, we estimate the presence of protuberances shifts the outer plate's centroid away from the centromere by tens of nanometers (~35 nm for stretched kinetochores shown in Fig. 3, B and C). Assuming that Mis12 is evenly distributed within the plate, such a shift would be responsible for ~45% of the Delta$_{CenpA-GFP–Mis12}$ value. Therefore, fluctuations in the shape of the kinetochore outer layer appear to significantly influence the value of Delta.

SHREC values are affected by the sample's structural preservation

Values of Delta$_{CenpA-GFP–Hec1}$ in our dataset (Fig. 1) are ~30% greater than the values previously reported in human cells (Wan et al., 2009). One prominent difference is that previous work used formaldehyde fixation, whereas we fix cells in glutaraldehyde to achieve a level of structural preservation required for EM. Labile structures often become structurally undetectable in EM after formaldehyde/methanol fixation (Melan and Sluder, 1992; McDonald, 1994), which suggests that at least some proteins become denatured. To determine whether this level of denaturation affects the

distribution of kinetochore proteins, we compared SHREC values for the same pairs of proteins in cells fixed with various fixatives.

For the first step we focused on the distributions of CenpT and Hec1, both of which can be reliably immunodetected after either glutaraldehyde or formaldehyde fixations (Fig. 4 A). We found that both the absolute values of Delta and the extent of the taxol-induced decrease in Delta are greater in the glutaraldehyde-fixed cells (Fig. 4 B). We also found that intrinsic mechanical properties of the kinetochore appear different in different fixatives as evident from the statistically significant differences in kinetochores' compliancy (Fig. 4 C). Currently, there are no data to determine whether the true live-cell compliancy is closer to the values observed in glutaraldehyde- versus formaldehyde-fixed cells.

The size (FWHM) of the fluorescent spots is also affected by the fixative. Both CenpT and Hec1 spots are smaller after glutaraldehyde versus formaldehyde fixation. Taxol treatment results in a highly significant increase of FWHM$_{Hec1}$ and a mild yet significant increase of FWHM$_{CenpT}$ in glutaraldehyde-fixed cells (Fig. 4 B). These changes are consistent with the idea of radial expansion and compaction of kinetochores (Magidson et al., 2015; Wynne and Funabiki, 2015). In contrast, FWHM is not statistically different in taxol versus control cells after formaldehyde fixation, and even control cell kinetochores appear larger than those in taxol-treated glutaraldehyde-fixed cells (Fig. 4 B). These data support the notion that partial denaturation of protein in formaldehyde-fixed cells make certain structural changes induced by taxol undetectable.

Similar effects are observed when SHREC parameters are measured for CenpA-GFP–Hec1. Noteworthy is that endogenous CenpA becomes accessible to the antibodies only after denaturing fixation, such as formaldehyde followed by methanol (Marshall et al., 2008). We found that relative to glutaraldehyde, this type of fixation decreases Delta$_{CenpA-GFP–Hec1}$ by ~35%. Indeed, after
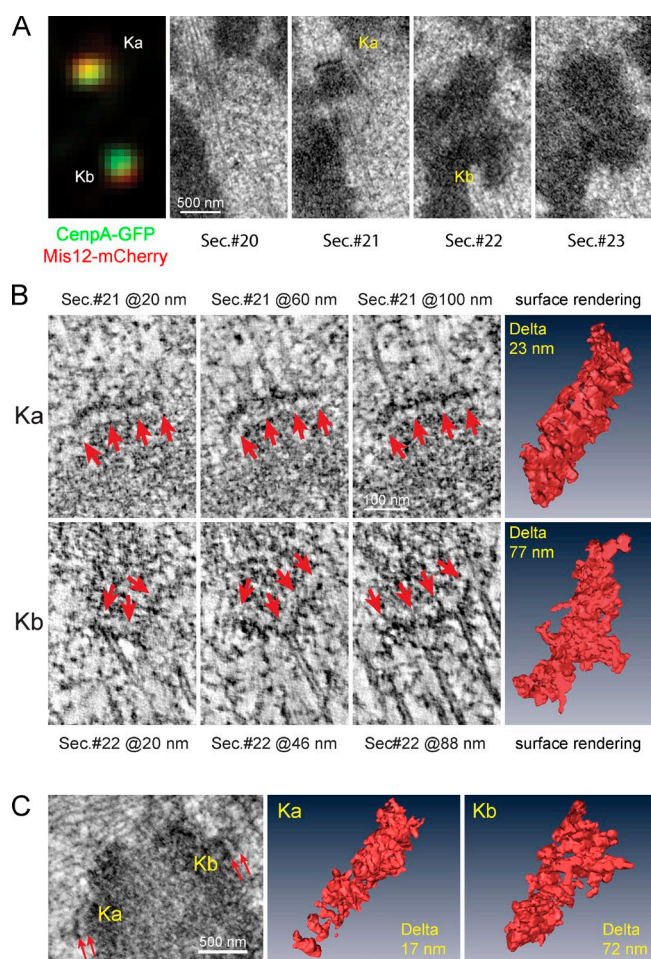
Figure 3. **Structural differences of low- versus high-Delta kinetochores during metaphase.** (A) Correlative LM and EM for a pair of sister kinetochores. Mis12-mCherry (red) and CenpA-GFP (green) fluorescence are shown in the left panel, and corresponding EM serial sections are shown in the remaining panels. (B) Slices from EM tomographic reconstructions of Ka and Kb shown in A. The three columns on the left are individual 2-nm-thin slices from the reconstructions of Ka (top) and Kb (bottom). The height of each slice within the tomogram is indicated. Arrows point at the electron-opaque outer plate. Images in the right column are surface renderings of the electron opaque outer layer segmented from the rest of the reconstruction volume. Delta values are indicated for each kinetochore. (C, left) A single EM section containing a different pair of sister kinetochores. (C, middle and right) Surface renderings of EM tomographic reconstructions of each sister kinetochore with Delta values indicated.

glutaraldehyde fixation, Delta$_{CenpA-GFP–Hec1}$ in taxol-treated cells appears to be greater than in control cells fixed with formaldehyde-methanol (Fig. S4). As expected, FWHM for both CenpA-GFP and Hec1 spots is significantly larger in formaldehyde-methanol fixed cells than in glutaraldehyde-fixed cells (Fig. S4). Interestingly, FWHM of the endogenous CenpA spot that can be visualized only after denaturing fixations is smaller than spots formed by other kinetochore proteins tested so far, and the size of this CenpA spot does not increase on taxol treatments (Fig. S4). This indicates a limited penetration of anti-CenpA antibodies into the heterochromatin even after the denaturing fixation (Marshall et al., 2008).

CenpT and Hec1 form complex multilobe distributions within the kinetochore

Thus far, our results suggest that values of Delta correlate with the shape of the outer kinetochore plate (Fig. 3). On taxol treatment,

kinetochores change orientation with respect to the centromere (Fig. 2), and their outer layers enlarge (Fig. 4); however, these changes are detectable only in glutaraldehyde-fixed cells (Fig. 4). To investigate whether shape changes that are likely to occur during taxol-induced reorganization of the kinetochore architecture make a significant contribution toward the value of Delta, we combined wide-field (WF) and 3D structured illumination (SI) microscopy. Delta was measured in WF images, whereas the shape of CenpT and Hec1 distributions within the same kinetochore was assessed in SI (Fig. 5 A).

SI reveals that both Hec1 and CenpT form spatially complex distributions in both control and taxol-treated metaphase cells (Fig. 5, B and C). In contrast to WF, where CenpT and Hec1 appear as individual round spots that overlap to a larger (low Delta) or smaller (high Delta) degree, SI reveals that individual kinetochores comprise multiple lobes of CenpT and Hec1. Even for kinetochores with Delta values <1 pixel (40 nm), many of these lobes do not colocalize and can be separated by distances resolvable in SI. In low-Delta kinetochores, CenpT often extends farther than Hec1 toward the attached microtubules, which shifts CenpT's center of mass (Fig. 5 B). In high-Delta kinetochores, Hec1 tends to form protuberances toward the K fiber (Fig. 5 B). Similar complex spatial patterns are observed in taxol-treated cells (Fig. 5 C). Therefore, the SI data are not consistent with the idea that taxol-induced changes in Delta reflect a decrease in the separation between the inner and outer kinetochore components.

Taxol arrests mitotic cells with unattached kinetochores

Although SI reveals that kinetochore shapes are highly variable in both control and taxol-treated metaphase cells, one particular type of morphology is seen only in taxol. A low number of kinetochores (1–5) in each taxol-treated cell ($n > 30$) expands into crescents that partially encircle the centromere. Formation of Hec1 is apparent in WF; however, SI demonstrates that CenpT also expands, albeit to a lesser degree (Fig. 5 A). Similar radial expansion of the outer kinetochore has been reported in the absence of end-on microtubule attachment (Hoffman et al., 2001; Magidson et al., 2015; Wynne and Funabiki, 2015). Indeed, most kinetochores in nocodazole-treated RPE1 are morphologically indistinguishable from the crescent kinetochores observed in taxol-treated cells (Fig. 6). This prompted us to investigate whether treatment of metaphase cells with taxol leads to detachment of microtubules from some of the kinetochores.

It has been shown previously that some kinetochores in taxol-arrested cells retain mitotic checkpoint proteins, such as Mad2 (Waters et al., 1998). Therefore, we followed mitotic progression in RPE1 cells with a single knocked-in allele of Mad2-Venus (Collin et al., 2013) treated with 10 μM taxol. Taxol was added when Mad2-Venus fluorescence had begun to decrease on the last positive kinetochore, which indicates that all kinetochores have established end-on attachments.

Thirteen of the 18 cells treated with taxol during metaphase exited from mitosis in 5–20 min. In these cells, Mad2-Venus either did not reappear at the kinetochores or its recruitment was transient and barely detectable (the signal to noise ratio in these low-light recordings was insufficient for quantitative measurements). The chromosomes were unable to move poleward in these cells and remained near the spindle equator, which indicates that microtubules were stabilized by taxol (Fig. 7 A). In five cells, the addition of taxol resulted in prominent recruitment of Mad2-Venus to a low number (1–3)
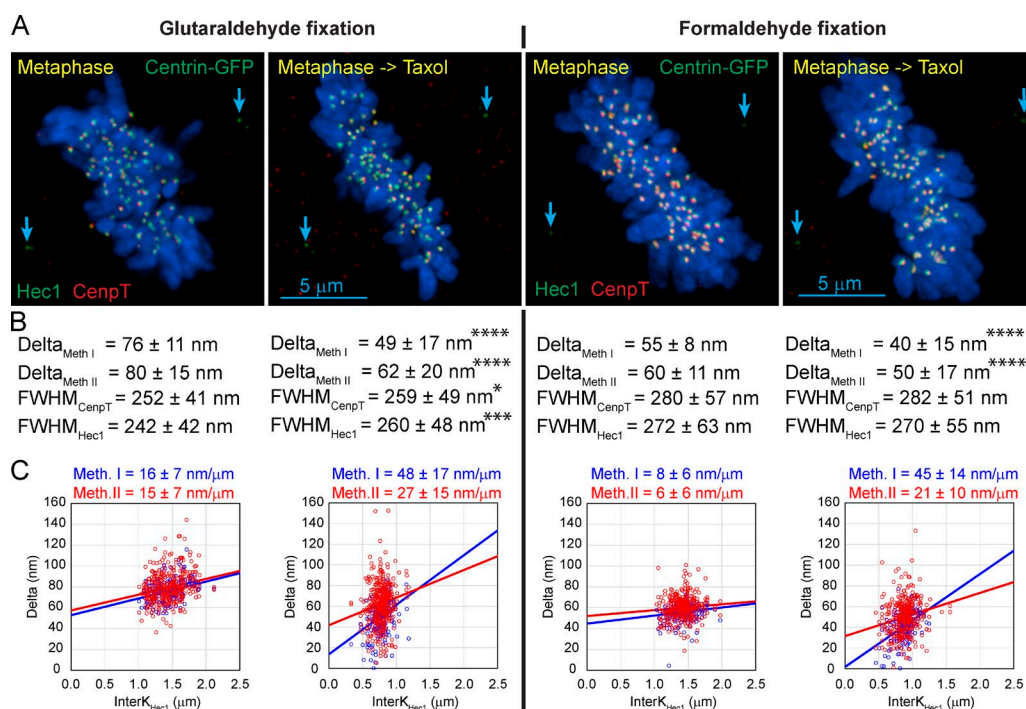
Figure 4. Effects of different fixatives on Delta, FWHM, and the apparent mechanical properties of kinetochores. (A) Control and taxol-treated metaphase RPE1 cells antibody immunostained for CenpT (red) and Hec1 (green) after fixation with glutaraldehyde (left) or formaldehyde (right). Location of the centrioles (Centrin-GFP) is marked by blue arrows. Notice that the chromosomes (visualized with Hoechst 33342) appear slightly swollen after formaldehyde fixation. (B) Delta values calculated by both methods I and II and FWHM values for CenpT and Hec1 are shown for each fixation condition under the corresponding image in A. Note that Delta is consistently lower in formaldehyde-fixed samples. Also notice a highly statistically significant change in FWHM of Hec1 in glutaraldehyde-fixed samples. FWHM of both CenpT and Hec1 are larger after formaldehyde fixation, and the values are not affected by taxol. Asterisks indicate statistical significance of mean value difference between control and taxol-treated cells as assessed by two-tailed t test (*, $P <$ 0.05; ***, $P <$ 0.001; ****, $P <$ 0.0001). (C) Scatterplots of Delta versus interkinetochore distance and the values of kinetochore compliance for each of the four conditions. Meth., method.

of kinetochores. This recruitment occurred within 5–10 min and by kinetochores different from the last kinetochore that lost Mad2 immediately before the addition of taxol (Fig. 7 B). Correlative LM/EM analysis demonstrates that the Mad2-Venus positive kinetochores lack end-on attachment to microtubules, are enlarged, and display a prominent corona (Fig. 7 C). In contrast, the sisters of Mad2-positive kinetochores and other kinetochores in the cells display end-on attached microtubules (Fig. 7 C). Therefore, taxol induces loss of end-on microtubule attachment on a low number of kinetochores, and only those cells that regain unattached kinetochores arrest in mitosis.

Discussion

Flexibility of kinetochore architecture

The assumption of layered-disc architecture is paramount for the interpretation of Delta values as true distances separating various intrakinetochore components. For complex spatial distributions, the meaning of the distance between the centroids is not apparent if the objects are malleable or the exact shapes are unknown.

The outer but not inner layers of unattached kinetochores have been shown to radially expand into crescents that encircle the centromere and compact on formation of microtubule attachments (McEwen et al., 1993; Thrower et al., 1996; Hoffman et al., 2001; Magidson et al., 2015; Wynne and Funabiki, 2015). The kinetochore expansion-compaction cycle involves both a structural reorganization and compositional changes. The amount of outer kinetochore proteins, including those

proteins that are directly involved in the formation of microtubule attachments (e.g., Hec1; Magidson et al., 2015), decreases significantly when end-on attachments are formed, and this decrease is likely to be an important contributor to the change in the kinetochore architecture (Fig. S5). The prominent architectural/compositional reorganization creates a substantial problem in comparing Delta values of attached versus unattached kinetochores. Within a circular segment, the distance between centroids of a crescent-like outer layer and the inner spot-like domain is not proportional to the distance between the molecules within these domains. In fact, formal application of SHREC to kinetochores in nocodazole-treated cells yields the lowest values of Delta, even though peripheral parts of the Hec1 crescents are clearly more distant from the CenpA spots than during metaphase when Delta is high (Fig. S5 A). Radial expansion may result in an apparent decrease in Delta when the separation between the components actually increases.

Our analysis of FWHM suggests that the outer kinetochore expands to a larger degree than the inner parts when cells are treated with taxol (Figs. 1 D and 4 B). This differential expansion of outer layers supports the idea that even attached mammalian kinetochores are shaped as radial segments with a narrow base and wider outer domains. Although conventional LM fails to resolve the shape of Hec1 distribution in control cells, the proteins that reside farther from the base of the kinetochore (e.g., CenpF and CenpE) appear as crescents as expected for a segment-shaped structure (Fig. S5 B). Further, SI LM demonstrates that even during metaphase, when the outer layers are most compact, spatial distributions
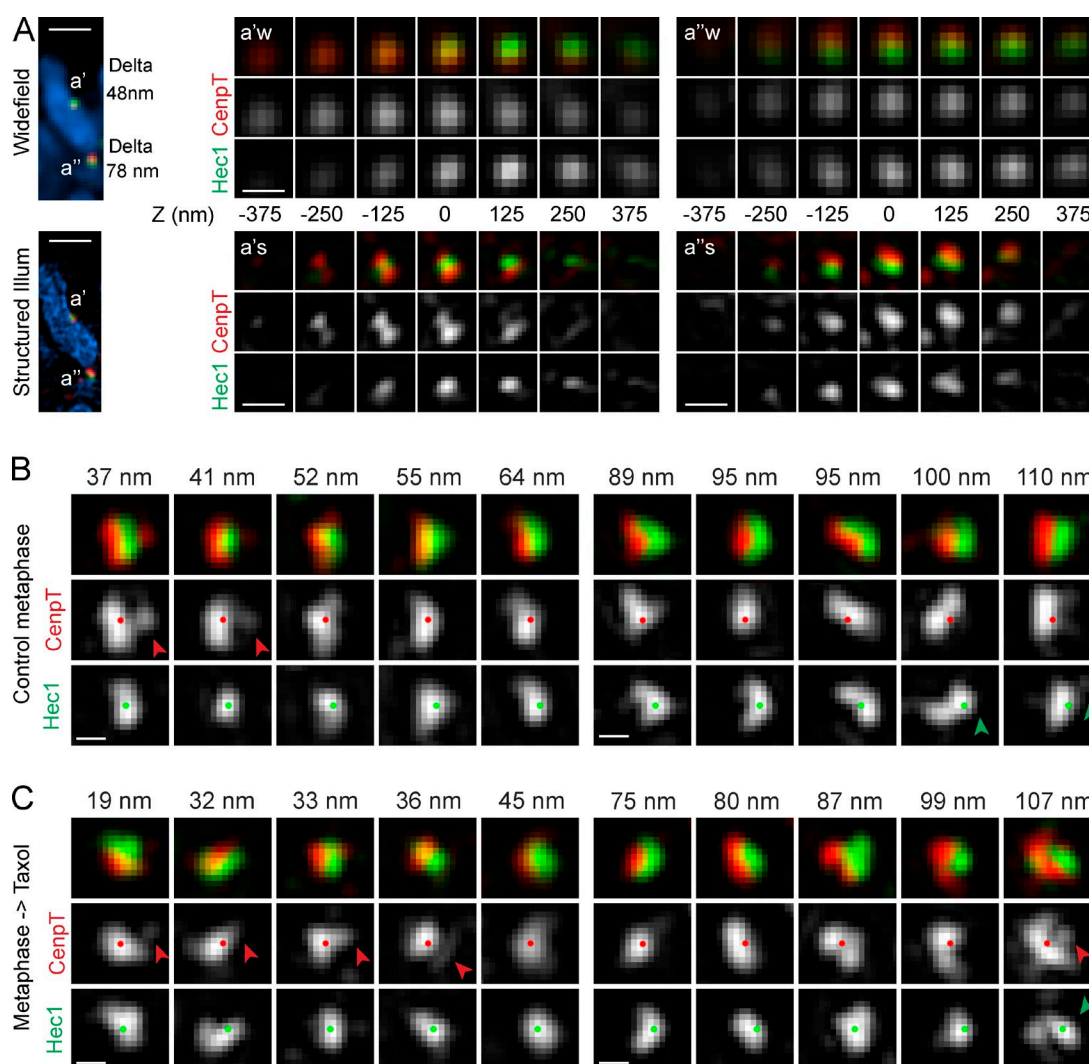
Figure 5. **Shapes of CenpT and Hec1 distributions visualized via SI microscopy.** (A) Direct comparison of conventional WF versus SI microscopy. In WF, microscopy (top) of sister kinetochores with lower (a′) and higher (a″) Delta appear as individual round spots of CenpT and Hec1 that are shifted with by the value of Delta with respect to one another. SI (bottom) reveals complex multilobe distributions of CenpT and Hec1 within the diffraction limited spots. Full optical Z series for each kinetochore are shown in both WF and SI. Distance for each plane from the central slice is indicated. Illum, illumination. Bars: (left) 1 μm; (right) 200 nm. (B and C) SI images of kinetochores (maximum intensity projections) representative of the low (left panels) versus high range of Delta values (right panels) in control (B) and taxol-treated (C) metaphase cells. The images are aligned so that the outer layer always faces to the right and centroids of CenpT (red dots) and Hec1 (green dots) separate along the horizontal axis. Red arrowheads denote lobes of CenpT that extend beyond Hec1 toward microtubules. Green arrowheads point at protuberances in the distribution of Hec1. Measured values of Delta (method II) are shown above the panels. Bars, 200 nm.

of individual proteins are more complex than simple narrow discs. For example, it is not unusual for individual lobes of CenpT to extend beyond Hec1 toward the attached microtubules (Fig. 5). This complex distribution, which is not apparent in conventional LM, is inconsistent with the conclusions of SHREC analysis that places CenpT ~60 nm deeper inside the kinetochore than Hec1.

Curiously, the expansion of the outer kinetochore that others and we see in unbound mammalian kinetochores was not detected by immuno-EM in unbound DT40 kinetochores (Suzuki et al., 2011). This could reflect a species variation because DT40 kinetochores are considerably smaller than human kinetochores and only bind three or four microtubules (Ribeiro et al., 2009). Furthermore, our results indicate that the fixation conditions used by Suzuki et al. (2011) are expected to result in a denatured and expanded kinetochore that could

mask the drug-induced expansion of the outer layer (Fig. 4, A and B; and Fig. S4). Interestingly, Suzuki et al. (2011) demonstrated that in in vitro assays, CenpT molecules are capable of unfolding and expanding more than twofold, which could explain the complex multilobed CenpT distributions we see in SI illumination (Fig. 5).

Effect of chemical fixation on kinetochore architecture and Delta values

An additional problem for interpretation of SHREC data is that the measurements are strongly affected by the structural preservation of the sample (Figs. 4 and S4). Because of diffraction-limited resolution of LM, little attention is usually paid to submicrometer-scale structural changes that occur during denaturing fixations. However, these changes may become prominent in superresolution LM modalities and consistent with this
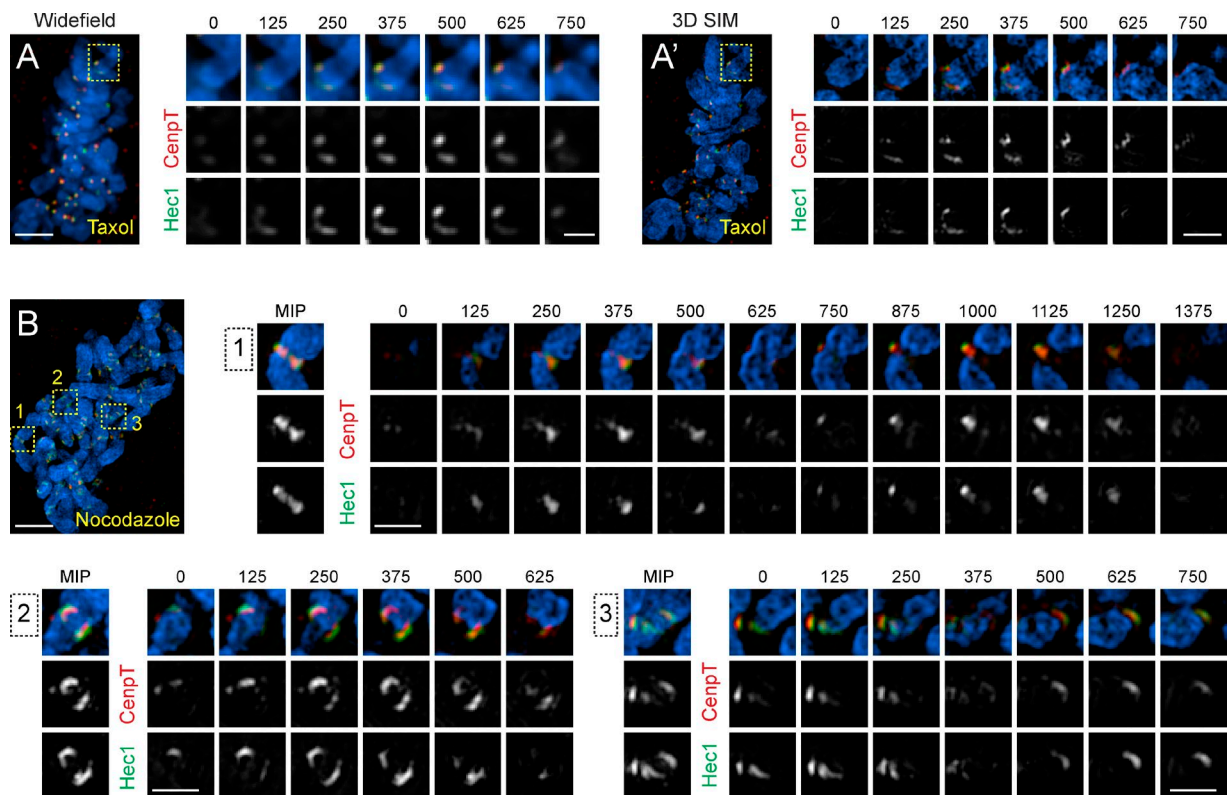
Figure 6. **Low number of kinetochores in taxol-treated cells display crescent-like morphology resembling unattached kinetochores.** (A and A′) WF (A) and structured-illumination (A′) images (maximum-intensity projection) of a taxol-treated metaphase cell stained for CenpT (red) and Hec1 (green). Full optical series through the centromere region of a chromosome (box) with an expanded crescent-like kinetochore is shown at higher magnification. Black numbers indicate height of each optical slice (nm) within the volume. One sister kinetochore is compact, whereas the outer layer (Hec1) of the sister forms an extended crescent. The difference in the organization of sister kinetochores is particularly prominent in SI microscopy. Bars: (main) 5 µm; (insets) 1 µm. (B) SI image (maximum intensity projection, MIP) of a metaphase cell treated with 3 µM nocodazole for 15 min during metaphase. Centromere regions of chromosomes from the boxed areas are shown at higher magnification. The outer kinetochores (Hec1) consistently form crescents that encircle the centromere. Formation of the crescents is not always apparent in planar views (maximum intensity projections) because of orientation of the centromere in space. However, expansion of the outer layer is consistently detected in complete optical series through the centromere region. Bars: (main) 5 µm; (insets) 1 µm.

notion that the absolute values of Delta differ significantly in glutaraldehyde- versus formaldehyde-fixed cells. We also find that only glutaraldehyde fixation is suitable for detecting the enlargement of the outer but not inner parts of the kinetochore on taxol treatment (Figs. 4 and S4) or during prometaphase (Figs. S5 C). The enlargement is evident from the increase in FWHM and is supported by the changes in the cumulative distribution of immunogold particles in the populations of aligned kinetochores (Figs. 2 and S5 C). In contrast, when fixed with formaldehyde, inner and outer kinetochores appear equally large in control and taxol-treated cells alike. The inability to detect the enlargement is consistent with the notion that the trilaminar plates morphology of the kinetochore became apparent in EM only on the use of glutaraldehyde fixation (Brinkley and Stubblefield, 1966). However, it is important to emphasize that a certain degree of structural disintegration occurs even in glutaraldehyde, as evident from the differences in the kinetochore morphology after chemical fixation versus high-pressure freezing and freeze substitution of mammalian cells (McEwen et al., 1998).

Interpretation of Delta values

Our data suggest that literal interpretation of SHREC Delta as a distance between the molecules within the mammalian kinetochores is poorly justified. Although SHREC can yield quantitative information for smaller and shapeless kinetochores in the budding yeast (Aravamudhan et al., 2015), prominent changes

in size, shape, and orientation of the outer kinetochore that occur in mammalian cells are likely to make a larger contribution into the value of Delta than changes in the relative positions and orientation of individual molecules, particularly after denaturing fixations. Caution is necessary in using SHREC to draw quantitative conclusions on the nanometer-scale architecture of kinetochores. Quantification of SHREC values is particularly difficult because Delta values calculated via alternative approaches to chromatic aberration correction may match or be significantly different under various conditions. For example, because of different sensitivity to changes in kTilt, elongation of certain components in response to taxol may not be apparent when method I is used (i.e., constant Delta under conditions that increase kTilt actually implies that the distance increases). On the other hand, for small Deltas, method II can significantly overestimate the real distance particularly when the variability of the distribution is high (Fig. S2). These uncertainties complicate comparisons between SHREC values and more direct approaches such as single-particle EM. For example, near-identical Delta values from Hec1 to Dsn1, Spc24, and Spc25 are in perfect agreement with the demonstration that Spc24 and Spc25 bind to Dsn1 (Petrovic et al., 2014). However, whereas SHREC positions Mis12 48 nm from Hec1, EM finds that the Mis12–Knl[12106-2316]–Ndc80 complex appears ~75 nm in length and structurally heterogeneous because of flexibility of the coil-coiled region of Ndc80.
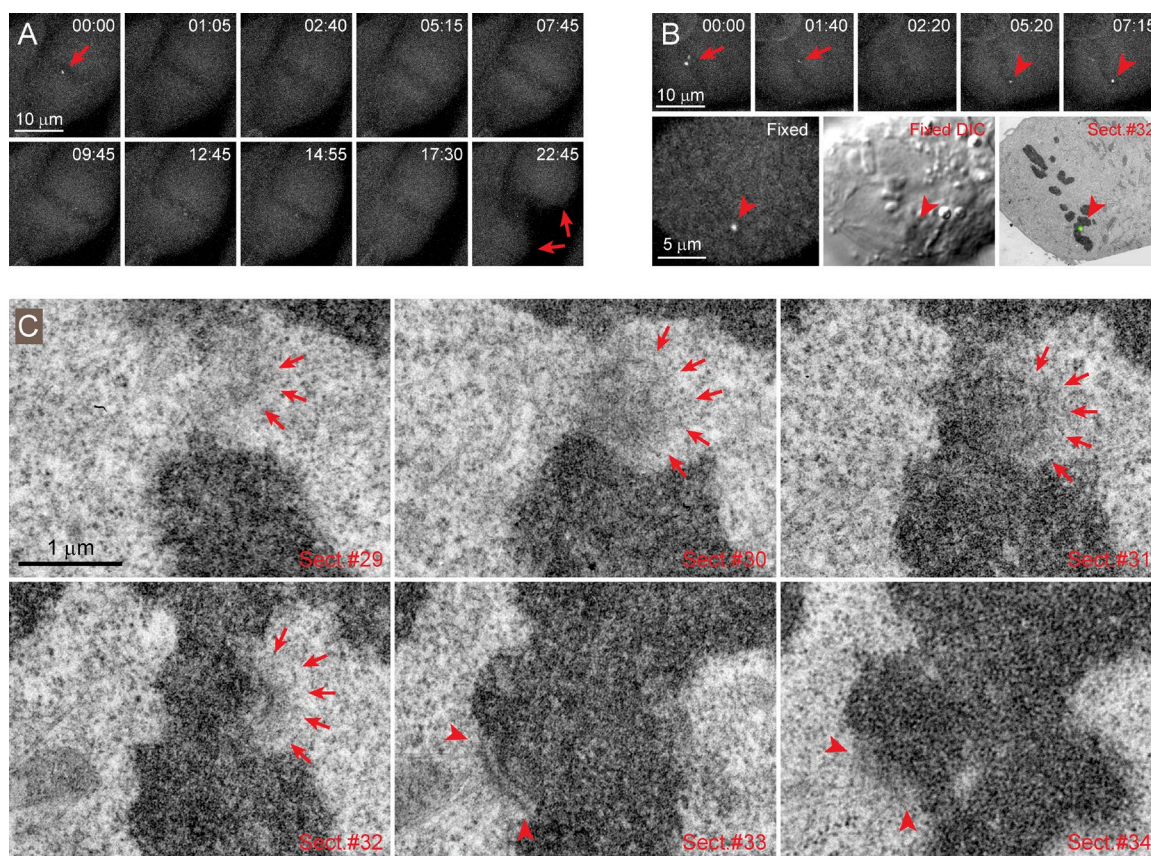
Figure 7. **Taxol induces loss of end-on microtubule attachments on a low number of kinetochores in metaphase cells.** (A) Time-lapse recording of a taxol-treated metaphase cell that exits from mitosis. In this cell, Mad2-Venus disappears from the last kinetochore (red arrow in frame 00:00) shortly after addition of taxol. The cell exits from mitosis ~15 min later and undergoes cytokinesis (red arrows in frame 22:45). Notice that because of stabilization of microtubules in taxol, chromosomes (seen as dark bodies in fluorescent background) do not move poleward but remain near the spindle equator during anaphase and telophase. (B) Time-lapse recording of a taxol-treated metaphase cell. In this cell, Mad2-Venus disappears from the last pair of kinetochores shortly after addition of taxol (red arrows in 00:00 and 01:40). Approximately 5 min later Mad2-Venus begins to accumulate at a different kinetochore (arrowheads in 05:20 and 07:15). This kinetochore is identified via correlative EM of this cell fixed shortly after 7:15. (C) Serial section (Sect.) EM demonstrates that the Mad2-Venus positive kinetochore completely lacks end-on microtubule attachments, and its electron-opaque corona partially encircles the centromere (arrows). In contrast, the sister kinetochore has a well-defined outer plate with several end-on attached microtubules (arrowheads).

Mechanisms of taxol-induced mitotic arrest

Two prominent changes occur within the kinetochores in taxol-treated cells. First, the relative orientation of the sister kinetochores becomes less reproducible. The means and SDs of the angles between the centromere and spindle (cTilt) as well as between the intrakinetochore axis and the centromere (kTilt) increase approximately threefold (Fig. 1 D). These changes are consistent with the idea that the spindle forces elastically stretch and orient both the centromere chromatin and the kinetochores. In contrast, the second change—the expansion of the outer kinetochore in response to the decrease in spindle forces—is uncharacteristic of an elastic Hookean system. A Hookean spring kinetochore would be stretched by attached microtubules and collapsed when the forces cease. Indeed, in untreated metaphase cells, kinetochores with large Delta display protuberances as if parts of the outer plate are pulled out by the attached microtubules. Counter to this observation, on average, the size of outer kinetochore is most compact when the force that stretches the centromere is maximal, whereas cessation of microtubule-based forces leads to the radial expansion of the kinetochore domain to which the force is directly applied. These complex dynamics imply that kinetochores should not be viewed as elastic springs.

An important property of the mammalian kinetochore is a large degree of independence in structural changes within the outer and inner kinetochore domains. The independent expansion of the outer layer accompanied by changes in stoichiometry of core kinetochore components, such as recruitment of additional Hec1 (Magidson et al., 2015), implies that new complexes are connected within the layer but not directly to the base. This organization is consistent with the previous structural reconstructions (Dong et al., 2007) and with the views on the organization of the kinetochore as a molecular lawn rather than a set of repetitive uniformly organized microtubule binding sites (Zaytsev et al., 2014).

If kinetochores are not elastic springs, then what is the mechanism of mitotic arrest induced by taxol? Here, we show that changes induced by taxol are insufficient to arrest mitotic progression unless unattached kinetochores reappear (Fig. 7). Our data do not rule out that a weaker wait-anaphase signal is produced in the cells even in the absence of Mad2-positive unattached kinetochores. In our experimental design, taxol is added to the cells during late metaphase. In the absence of taxol, these cells are expected to initiate anaphase in ~5 min, but we observe a modest 5- to 15-min delay in most cells (~10 min in Fig. 7 A). This observation is consistent with observations of Clute and Pines

(1999), who showed that addition of taxol to late-prometaphase HeLa and PtK$_1$ cells rapidly stops degradation of cyclin-B and arrests mitotic progression. However, we find that mitotic delay is sustained only for a short time if cells fail to rerecruit Mad2 to at least a single kinetochore. Therefore, it appears that tension plays only a minor role in the release of the mitotic checkpoint, whereas a single unattached kinetochore is known to arrest mitotic progression for hours (Rieder et al., 1994, 1995). However, slower mitotic progression in the absence of tension may be important by allowing cells time to accumulate unattached kinetochores. Noteworthy is that mitotic arrest is observed in all cells when taxol is added ∼30 min before anaphase onset (Clute and Pines, 1999) but in only approximately one third of the cells when the drug is added just before anaphase.

Micromanipulation experiments reveal that tension at the kinetochore or at the centromere plays an important role in stabilization of end-on microtubule attachments (Nicklas et al., 2001); however, the exact mechanism that converts mechanical factors into molecular regulation of microtubule stability remains elusive. Our experiments demonstrate taxol treatment also increases the degree of fragmentation of Hec1 and CenpT domains in kinetochores (Figs. 5 and 6), which in turn may destabilize microtubule attachment. It remains to be determined if the structural changes we observe in taxol-treated cells cause or are a consequence of reduced tension or the consequence of some other effect of the drug.

Materials and methods

Cell culture and drug treatments

hTERT RPE1 cells (Clontech) and all derivative clones were cultured in DMEM supplemented with 10% FCS (Life Technologies) at 37°C and 5% CO$_2$. Full-length CenpA and Centrin-1, fused to GFP, were introduced to RPE1 cells sequentially via lentivirus transfection in the Lentilox 3.1 vector under unregulated cytomegalovirus promoter. The stable clone isolated from the transfected population has been described in our previous work (Magidson et al., 2011; Sikirzhytski et al., 2014). RPE1 clones coexpressing centrin1-GFP and full-length Mis12 fused to mCherry were generated by two rounds of lentivirus transfections: centrin1-GFP was introduced in the first round, and cells with appropriate level of expression were isolated by FACS sorting. Mis12-mCherry in the Lentilox3.1 vector was then transfected into these selected cells. Final clones with the sufficient brightness of Mis12 at the kinetochores were isolated by two rounds of limited-dilution cloning. For all imaging analyses cells were grown on 11/2 (170-µm-thick) coverslips for 2–4 d. Only relatively flat cells with favorable orientation of the spindle were chosen for analyses.

For fixed-cell characterization of kinetochore, architecture taxol (10 µM in DMSO) or nocodazole (3 µM in DMSO) were added ∼15 min before fixation. In live-cell checkpoint reactivation experiments (Fig. 7) 10 µM taxol (in DMSO) was added when the cell contained a single Mad2-positive kinetochore.

Antibody labeling

For correlative immuno-LM/EM analyses (Figs. 1, 2, and 3; and Figs. S1 and S2 C), cells were concurrently permeabilized and fixed in warm PEM buffer (100 mM Pipes, pH 6.9, 2.5 mM EGTA, and 5 mM MgCl$_2$, pH 6.9) supplemented with 1% Triton X-100 and 1% glutaraldehyde (EM grade; Sigma-Aldrich) for 20 min. For LM analyses, cells were permeabilized in an identical manner except in some experiments 3.2% paraformaldehyde (EM grade; EMS) was used instead of glutaraldehyde. In the experiments that involved immunostaining for endogenous

CenpA, formaldehyde fixation was shortened to 5 min, and the coverslips were postfixed in 100% methanol at –18°C for 15 min.

Hec1 was visualized using the 9G3 monoclonal antibody (Abcam) at 1:300. For correlative LM/EM datasets, FluroNanogold anti–mouse Fab' Alexa Fluor 594 (Nanoprobes) was used as a secondary antibody. In LM-only datasets, secondary antibodies conjugated with either Alexa Fluor 594 or 488 were used (Life Technologies).

CenpT was visualized with a rabbit polyclonal antibody provided by I. Cheeseman (Massachusetts Institute of Technology, Cambridge, MA) at 1:400. Specificity of this antibody has been characterized (Gascoigne and Cheeseman, 2013). Alexa Fluor 594 secondary antibody was used.

Endogenous CenpA was visualized with the 3–19 mouse monoclonal antibody (Abcam) at 1:200. Although both 3–19 (CenpA) and 9G3 (Hec1) antibodies are mouse monoclonal, we were able to obtain specific localization of these proteins by using isoform-specific secondary antibodies. 3–19 was followed by a γ1b-specific antibody conjugated to Alexa Fluor 488, and 9G3 was followed by a γ2a-specific antibody conjugated to Alexa Fluor 594.

CenpF was visualized with a rabbit polyclonal antibody against a C-terminal peptide (NB500-101; Novus Biological) at 1:400.

Conventional LM imaging

Multimode 3D datasets of immunostained cells (red FluoroNanogold and green GFP fluorescence as well as differential interference contrast [DIC] images) were collected in spinning disc confocal mode on a Revolution microscopy workstation (Andor) with Nikon 100× NA 1.4 PlanApo VC lens and Yokohama GSU-22 scanner. Images were captured with the Andor iXon-885 EM charge coupled device camera at 55-nm X-Y pixel size and 200-nm Z steps. The system was controlled by Andor iQ2 imaging software.

For multicolor LM-only analysis of kinetochore architecture and for correlative SHREC/EM tomography and correlative GFP/serial-section EM analyses, WF images were recorded on a DeltaVision imaging system (Applied Precision) with 100× NA 1.35 lens (Olympus). These images were captured with the Photometrics CH-350 charge coupled device camera at 69-nm X-Y pixel size and 200-nm steps.

All raw images were deconvolved with the SoftWoRx 5.0 deconvolution software (Applied Precision), and objective lens-specific in-house recorded point-spread functions. Chromatic alignment of all microscopes was verified by recording Z series of 100-nm TetraSpeck microspheres (Life Technologies).

Structured Illumination LM

Superresolution 3D structured illumination microscopy images were acquired on a DeltaVision OMX SR (GE Healthcare) equipped with a 60×/1.42 NA PlanApo oil immersion lens (Olympus), 405-, 488-, 568-, and 640-nm solid-state lasers, and sCMOS cameras (pco.edge). Image stacks of 5–6 µm with 0.125-µm-thick Z sections and 15 images per optical slice (three angles and five phases) were acquired using immersion oil with a refractive index 1.518. Images were reconstructed using Wiener filter settings of 0.003 and optical transfer functions measured specifically for each channel with SoftWoRx 6.5.1 (GE Healthcare) to obtain superresolution images with a twofold increase in resolution both axially and laterally. Images from different color channels were registered using parameters generated from a gold grid registration slide (GE Healthcare) with the routines available in SoftWoRx 6.5.1.

Sample processing for correlative immuno-LM/EM

After collecting fluorescence images, the cells were postfixed in 1% glutaraldehyde (Sigma-Aldrich) in PBS, pH 7.4–7.6. 1.4-nm gold seeds

on the FluroNanogold secondary label for Hec1 were enhanced using the Gold Enhance EM kit (Nanoprobes) according to the protocol used by He et al. (2007), with minor modifications. Proper execution of gold enhancement procedures proved to be critical for obtaining a sufficient number of gold particles at the kinetochores (>10 per kinetochore) with acceptable levels of background. Samples were washed 3 × 5 min with PBS-glycine (20 mM sodium phosphate, pH 7.4, 150 mM NaCl, and 50 mM glycine) to quench unbound aldehydes and then washed 3 × 5 min with 5 mM sodium phosphate, pH 5.5, and 100 mM NaCl. Gold enhancement was performed in a dark room using solutions A (enhancer), B (activator), C (initiator), and D (buffer) from the Gold Enhance EM kit according to the following regiment. First, coverslips were placed on a mixture of the manufacturer's solutions A and B at a 1:1 ratio (40 µl each). After 5 min, coverslips were transferred onto a mixture of solutions C and D with 1:1 ratio (40 µl each) at 4°C. After 30 min of development, samples were transferred to 1–2% sodium thiosulfate to stop the further growth of gold particles. We found that enhancement at 4°C gave a more uniformed gold size and less background labeling than enhancement at RT. After gold enhancement, cells were washed 3 × 5 min with solution E, fixed in 1–2% glutaraldehyde in PBS, pH 7.4–7.6, and prepared for EM as previously described (Rieder and Cassels, 1999), except that osmium fixation and tannic acid treatment were omitted. For dehydration, coverslips were passed through a concentration series of ethanol at RT (5 min in 20%, 5 min in 50%, overnight in 70%, 10 min in 80%, 10 min in 96%, and three times by 10 min in 100% ethanol). Then the coverslips were directly transferred to pure acetone for 10 min and infiltrated with aceton/epon in steps of 3:1 (1 h); 1:1 (1 h); 1:3 (overnight), and pure resin (1 h) twice. The resin was polymerized at 60ºC for 48 h. 200-nm serial sections were obtained on an Ultracut UCT microtome (Leica) and collected on formvar-coated copper single-slot grids.

Images of 200-nm-thick sections were collected on a 1400 microscope (JEOL) operating at 120 kV. Correlation between morphologic features conspicuous in fluorescence, DIC, and EM images were used to match the orientation and z positions for individual focal planes, and then fluorescence images were overlaid on the EM reconstruction to determine exact positions of kinetochores.

Sample processing for correlative LM/EM and EM tomography

EM embedment procedures are detailed in Rieder and Cassels (1999). After collection of LM datasets, coverslips with fixed cells were rinsed in PBS, postfixed in 1% OsO$_4$ for 60 min, and then rinsed three times with deionized water water. Then, the coverslips were dehydrated using ethanol solutions at RT, following the same regiment as for immuno-EM embedment (see previous section). Complete series of 100-nm-thin or 200-nm-thick sections were obtained on an Ultracut UCT microtome and collected on formvar-coated copper single-slot grids. Thin sections were imaged on a 910 electron microscope at the accelerating voltage of 80 kV (Carl Zeiss). Images were captured on film and subsequently digitized with a flatbed scanner. Dual-tilt tomography series of selected thick sections were collected automatically, on an FEI Tecnai F20 electron microscope with a Gatan 2K×2K camera at the pixel size of 1.6 nm. The system was controlled by Serial EM software. Tilt series images were aligned using 10-nm colloidal gold particles deposited on the section surface as fiducial markers. Image alignment and 3D reconstruction were computed using IMOD (Kremer et al., 1996; Mastronarde, 1997).

Measurements of fluorescent spots

Procedures to characterize fluorescent spots that correspond to the inner and outer parts of kinetochores were implemented as interactive graphical user interface scripts in MATLAB (MathWorks). A compiled version of the software that runs on Microsoft Windows computers (requires MATLAB runtime environment available free of charge) and the original MATLAB scripts (tested on MATLAB 2014) are available in the online supplemental material.

All kinetochores in each analyzed cell were manually assigned individual identifiers (44–47 kinetochore pairs per cell). The subsequent steps were executed via the MATLAB script run for each kinetochore. First, a 20 × 20 × 7 pixel region of interest (ROI) was created around the central voxel selected by the operator. The local background value (lowest pixel value within the ROI) was subtracted. The volume was then segmented at 50% intensity of the peak corresponding to the selected kinetochore. The segmented image was displayed on the screen giving the operator an opportunity to assess whether the kinetochore was sufficiently discriminated from the neighboring kinetochores. Kinetochores that did not completely separate from their neighbors after segmentation were discarded.

x-y coordinates of the centroids were determined by nonlinear fitting (*lsqcurvefit* MATLAB function) in projections of the segmented volume with 2D Gaussian function. The fitting was done in two rounds: first with a symmetric five-parameter Gaussian to produce initial estimations for the subsequent fitting with a seven-parameter asymmetric Gaussian function. z coordinates of the kinetochore were estimated separately in x-z projections of the ROI. We opted for this approach instead of a single 3D Gaussian fit because of a need to directly correlate LM and EM datasets. Immuno-EM of thick sections automatically yields planar projections of the 3D volume within each 200-nm-thick section. Further, projections of the adjacent EM sections had to be used in most cases to ensure that the full spread of gold particles within sister kinetochores is captured.

FWHM for the fluorescent spots was approximated as 2.3548σ of the fit function (http://mathworld.wolfram.com/GaussianFunction .html). Only the larger of the two σ values of the asymmetric 2D Gaussian was used in the characterizations of spot sizes (Figs. 2 D and 3 C).

Alignment of correlative LM/EM datasets and averaging of aligned kinetochores

Images of individual kinetochores were rotated to fix the orientation of attached K fibers along the horizontal axis. Centroids of gold particle distributions that delineate Hec1 were calculated. Size and density variations among individual gold particles were ignored, and each particle was treated as a negligibly small binary spot. The EM images of individual kinetochores were then stacked so that the calculated gold-particle centroids were coincident. Fluorescence LM images were rotated by the same degree as the corresponding EM images and registered after rotation to achieve coincidence of Hec1 fluorescence centroids. The images of individual aligned kinetochores were stacked, and mean intensity projections were computed for each channel. Direct measurements of Delta and FWHM$_{Hec1}$ in the averaged fluorescence images yielded values that are statistically indistinguishable from the mean values in the larger LM dataset of unaligned kinetochores. This consistency supports the validity of the alignment technique used to prepare the averages. Because of variability of kTilt in prometaphase and particularly in taxol-treated cells (Fig. 3 B″), determination of FWHM$_{CenpA}$ in the averaged images of kinetochores with aligned Hec1 centroids is not meaningful.

Estimation of method I and method II accuracy

We use the random number generator of MATLAB (randn function) to generate normal distributions with defined mean and SD. A specified number of sister kinetochore pairs are generated and positioned on a plane so that the mean values and SDs of interkinetochore distances, Delta, kTilt, and cTilt all match the values specified by the operator.

Positions of the outer kinetochores are then shifted by specified values in x and y, which mimic the effect of chromatic aberration. Delta values are then automatically measured in the model cell according to methods I and II, and the means and SDs of the measured values are calculated. Comparison of the measured versus nominal values allows us to estimate the accuracy of each method under various conditions. The MATLAB script to run this simulation is available in the supplemental material.

Preparation of illustrations

LM images were scaled without interpolation in ImageJ to match the final magnification of EM images at 300 DPI. Contrast and brightness of the final images were adjusted in Adobe Photoshop CS4, and the figures were assembled in Adobe Illustrator CS4 (Adobe Systems). 3D renderings of the tomographic reconstruction in Fig. 3 were created using Amira 5.3.3 (Visage Imaging). Graphs were prepared in MAT-LAB or Excel (Microsoft) and imported into Illustrator as a PDF.

Online supplemental material

Fig. S1 illustrates the correlative LM/EM approach to characterization of kinetochore organization. Fig. S2 presents estimation of accuracy for alternative approaches to Delta measurements. Fig. S3 demonstrates morphologic variability of kinetochore structure in EM. Additional examples of changes in Delta values as a result of fixation conditions are shown in Fig. S5. Fig. S6 illustrates radial expansion of the kinetochores and its effects on values of Delta. A ZIP file with custom routines for measuring SHREC parameters and predicting accuracy of delta measurements via alternative approaches is also available. Online supplemental material is available at http://www.jcb.org/cgi/content/full/jcb.201412139/DC1.

References

Aravamudhan, P., A.A. Goldfarb, and A.P. Joglekar. 2015. The kinetochore encodes a mechanical switch to disrupt spindle assembly checkpoint signalling. *Nat. Cell Biol.* 17:868–879. http://dx.doi.org/10.1038/ncb3179

Brinkley, B.R., and E. Stubblefield. 1966. The fine structure of the kinetochore of a mammalian cell in vitro. *Chromosoma.* 19:28–43. http://dx.doi.org/10.1007/BF00332792

Cheeseman, I.M. 2014. The kinetochore. *Cold Spring Harb. Perspect. Biol.* 6:a015826. http://dx.doi.org/10.1101/cshperspect.a015826

Churchman, L.S., and J.A. Spudich. 2012. Single-molecule high-resolution colocalization of single probes. *Cold Spring Harb. Protoc.* 2012:242–245. http://dx.doi.org/10.1101/pdb.prot067926

Clute, P., and J. Pines. 1999. Temporal and spatial control of cyclin B1 destruction in metaphase. *Nat. Cell Biol.* 1:82–87. http://dx.doi.org/10.1038/10049

Collin, P., O. Nashchekina, R. Walker, and J. Pines. 2013. The spindle assembly checkpoint works like a rheostat rather than a toggle switch. *Nat. Cell Biol.* 15:1378–1385. http://dx.doi.org/10.1038/ncb2855

Dong, Y., K.J. Vanden Beldt, X. Meng, A. Khodjakov, and B.F. McEwen. 2007. The outer plate in vertebrate kinetochores is a flexible network with multiple microtubule interactions. *Nat. Cell Biol.* 9:516–522. http://dx.doi.org/10.1038/ncb1576

Dumont, S., E.D. Salmon, and T.J. Mitchison. 2012. Deformations within moving kinetochores reveal different sites of active and passive force generation. *Science.* 337:355–358. http://dx.doi.org/10.1126/science.1221886

Gascoigne, K.E., and I.M. Cheeseman. 2013. CDK-dependent phosphorylation and nuclear exclusion coordinately control kinetochore assembly state. *J. Cell Biol.* 201:23–32. http://dx.doi.org/10.1083/jcb.201301006

He, W., C. Kivork, S. Machinani, M.K. Morphew, A.M. Gail, D.B. Tesar, N.E. Tiangco, J.R. McIntosh, and P.J. Bjorkman. 2007. A freeze substitution fixation-based gold enlarging technique for EM studies of endocytosed Nanogold-labeled molecules. *J. Struct. Biol.* 160:103–113. http://dx.doi.org/10.1016/j.jsb.2007.07.004

Hoffman, D.B., C.G. Pearson, T.J. Yen, B.J. Howell, and E.D. Salmon. 2001. Microtubule-dependent changes in assembly of microtubule motor proteins and mitotic spindle checkpoint proteins at PtK1 kinetochores. *Mol. Biol. Cell.* 12:1995–2009. http://dx.doi.org/10.1091/mbc.12.7.1995

Kremer, J.R., D.N. Mastronarde, and J.R. McIntosh. 1996. Computer visualization of three-dimensional image data using IMOD. *J. Struct. Biol.* 116:71–76. http://dx.doi.org/10.1006/jsbi.1996.0013

Magidson, V., C.B. O'Connell, J. Lončarek, R. Paul, A. Mogilner, and A. Khodjakov. 2011. The spatial arrangement of chromosomes during prometaphase facilitates spindle assembly. *Cell.* 146:555–567. http://dx.doi.org/10.1016/j.cell.2011.07.012

Magidson, V., R. Paul, N. Yang, J.G. Ault, C.B. O'Connell, I. Tikhonenko, B.F. McEwen, A. Mogilner, and A. Khodjakov. 2015. Adaptive changes in the kinetochore architecture facilitate proper spindle assembly. *Nat. Cell Biol.* 17:1134–1144. http://dx.doi.org/10.1038/ncb3223

Manning, A.L., S.F. Bakhoum, S. Maffini, C. Correia-Melo, H. Maiato, and D.A. Compton. 2010. CLASP1, astrin and Kif2b form a molecular switch that regulates kinetochore-microtubule dynamics to promote mitotic progression and fidelity. *EMBO J.* 29:3531–3543. http://dx.doi.org/10.1038/emboj.2010.230

Maresca, T.J., and E.D. Salmon. 2010. Welcome to a new kind of tension: translating kinetochore mechanics into a wait-anaphase signal. *J. Cell Sci.* 123:825–835. http://dx.doi.org/10.1242/jcs.064790

Marshall, O.J., A.T. Marshall, and K.H. Choo. 2008. Three-dimensional localization of CENP-A suggests a complex higher order structure of centromeric chromatin. *J. Cell Biol.* 183:1193–1202. http://dx.doi.org/10.1083/jcb.200804078

Mastronarde, D.N. 1997. Dual-axis tomography: an approach with alignment methods that preserve resolution. *J. Struct. Biol.* 120:343–352. http://dx.doi.org/10.1006/jsbi.1997.3919

McDonald, K.L. 1994. Electron microscopy and EM immunocytochemistry. *Methods Cell Biol.* 44:411–444. http://dx.doi.org/10.1016/S0091-679X(08)60926-7

McEwen, B.F., J.T. Arena, J. Frank, and C.L. Rieder. 1993. Structure of the colcemid-treated PtK1 kinetochore outer plate as determined by high voltage electron microscopic tomography. *J. Cell Biol.* 120:301–312. http://dx.doi.org/10.1083/jcb.120.2.301

McEwen, B.F., C.E. Hsieh, A.L. Mattheyses, and C.L. Rieder. 1998. A new look at kinetochore structure in vertebrate somatic cells using high-pressure freezing and freeze substitution. *Chromosoma.* 107:366–375. http://dx.doi.org/10.1007/s004120050320

Melan, M.A., and G. Sluder. 1992. Redistribution and differential extraction of soluble proteins in permeabilized cultured cells. Implications for immunofluorescence microscopy. *J. Cell Sci.* 101:731–743.

Nicklas, R.B., J.C. Waters, E.D. Salmon, and S.C. Ward. 2001. Checkpoint signals in grasshopper meiosis are sensitive to microtubule attachment, but tension is still essential. *J. Cell Sci.* 114:4173–4183.

Petrovic, A., S. Mosalaganti, J. Keller, M. Mattiuzzo, K. Overlack, V. Krenn, A. De Antoni, S. Wohlgemuth, V. Cecatiello, S. Pasqualato, et al. 2014. Modular assembly of RWD domains on the Mis12 complex underlies outer kinetochore organization. *Mol. Cell.* 53:591–605. http://dx.doi.org/10.1016/j.molcel.2014.01.019

Ribeiro, S.A., J.C. Gatlin, Y. Dong, A. Joglekar, L. Cameron, D.F. Hudson, C.J. Farr, B.F. McEwen, E.D. Salmon, W.C. Earnshaw, and P. Vagnarelli. 2009. Condensin regulates the stiffness of vertebrate centromeres. *Mol. Biol. Cell.* 20:2371–2380. http://dx.doi.org/10.1091/mbc.E08-11-1127

Rieder, C.L. 1982. The formation, structure, and composition of the mammalian kinetochore and kinetochore fiber. *Int. Rev. Cytol.* 79:1–58. http://dx.doi.org/10.1016/S0074-7696(08)61672-1

Rieder, C.L., and G. Cassels. 1999. Correlative light and electron microscopy of mitotic cells in monolayer cultures. *Methods Cell Biol.* 61:297–315. http://dx.doi.org/10.1016/S0091-679X(08)61987-1

Rieder, C.L., A. Schultz, R. Cole, and G. Sluder. 1994. Anaphase onset in vertebrate somatic cells is controlled by a checkpoint that monitors sister kinetochore attachment to the spindle. *J. Cell Biol.* 127:1301–1310. http://dx.doi.org/10.1083/jcb.127.5.1301

Rieder, C.L., R.W. Cole, A. Khodjakov, and G. Sluder. 1995. The checkpoint delaying anaphase in response to chromosome monoorientation is mediated by an inhibitory signal produced by unattached kinetochores. *J. Cell Biol.* 130:941–948. http://dx.doi.org/10.1083/jcb.130.4.941

Sacristan, C., and G.J. Kops. 2015. Joined at the hip: kinetochores, microtubules, and spindle assembly checkpoint signaling. *Trends Cell Biol.* 25:21–28. http://dx.doi.org/10.1016/j.tcb.2014.08.006

Sikirzhytski, V., V. Magidson, J.B. Steinman, J. He, M. Le Berre, I. Tikhonenko, J.G. Ault, B.F. McEwen, J.K. Chen, H. Sui, et al. 2014. Direct kinetochore-spindle pole connections are not required for chromosome segregation. *J. Cell Biol.* 206:231–243. http://dx.doi.org/10.1083/jcb.201401090

Suzuki, A., T. Hori, T. Nishino, J. Usukura, A. Miyagi, K. Morikawa, and T. Fukagawa. 2011. Spindle microtubules generate tension-dependent changes in the distribution of inner kinetochore proteins. *J. Cell Biol.* 193:125–140. http://dx.doi.org/10.1083/jcb.201012050

Thrower, D.A., M.A. Jordan, and L. Wilson. 1996. Modulation of CENP-E organization at kinetochores by spindle microtubule attachment. *Cell Motil. Cytoskeleton.* 35:121–133. http://dx.doi.org/10.1002/(SICI)1097-0169(1996)35:2<121::AID-CM5>3.0.CO;2-D

Uchida, K.S., K. Takagaki, K. Kumada, Y. Hirayama, T. Noda, and T. Hirota. 2009. Kinetochore stretching inactivates the spindle assembly checkpoint. *J. Cell Biol.* 184:383–390. http://dx.doi.org/10.1083/jcb.200811028

Varma, D., X. Wan, D. Cheerambathur, R. Gassmann, A. Suzuki, J. Lawrimore, A. Desai, and E.D. Salmon. 2013. Spindle assembly checkpoint proteins are positioned close to core microtubule attachment sites at kinetochores. *J. Cell Biol.* 202:735–746. http://dx.doi.org/10.1083/jcb.201304197

Wan, X., R.P. O'Quinn, H.L. Pierce, A.P. Joglekar, W.E. Gall, J.G. DeLuca, C.W. Carroll, S.T. Liu, T.J. Yen, B.F. McEwen, et al. 2009. Protein architecture of the human kinetochore microtubule attachment site. *Cell.* 137:672–684. http://dx.doi.org/10.1016/j.cell.2009.03.035

Waters, J.C., R.H. Chen, A.W. Murray, and E.D. Salmon. 1998. Localization of Mad2 to kinetochores depends on microtubule attachment, not tension. *J. Cell Biol.* 141:1181–1191. http://dx.doi.org/10.1083/jcb.141.5.1181

Wynne, D.J., and H. Funabiki. 2015. Kinetochore function is controlled by a phospho-dependent coexpansion of inner and outer components. *J. Cell Biol.* 210:899–916. http://dx.doi.org/10.1083/jcb.201506020

Zaytsev, A.V., L.J. Sundin, K.F. DeLuca, E.L. Grishchuk, and J.G. DeLuca. 2014. Accurate phosphoregulation of kinetochore-microtubule affinity requires unconstrained molecular interactions. *J. Cell Biol.* 206:45–59. http://dx.doi.org/10.1083/jcb.201312107